

Mechanostat-type effective density correction for Carter-Hayes growth: application to topology optimization and its efficient interpolation for a target strain energy and volume fraction

Luis Irastorza-Valera^a, Ricardo Larraínzar-Garijo^{b,c}, Javier Montoya-Adárraga^b, Luis Saucedo-Mora^a

^a *E.T.S. de Ingeniería Aeronáutica y del Espacio, Universidad Politécnica de Madrid, Pza. Cardenal Cisneros 3, 28040 Madrid, Spain*

^b *Orthopaedics and Trauma Department, Hospital Universitario Infanta Leonor, C/ Gran Vía del Este 80, 28031 Madrid, Spain*

^c *Surgery Department, Faculty of Medicine, Universidad Complutense de Madrid, Pl. de Ramón y Cajal s/n, 28040 Madrid, Spain*

Abstract

In automotive and aerospace industries, the need for optimized structures offering the best mechanical performance for the minimum weight is ubiquitous. To that aim, Topology optimization (TO) is a very popular structural design tool. Particularly, the Solid Isotropic Material with Penalization (SIMP) method offers a trade-off between minimum compliance (i.e., maximum stiffness) and a fixed amount material for a given set of static, deterministic boundary conditions. Since TO is a non-convex problem, its gradient can be tuned by filtering the topology's contour, creating sharper material profiles without necessarily compromising optimality. However, despite simplifying the layout, some filters fail to address manufacturability concerns such as capillarity (thin tweaks as struts) generated by uncertain loading, vibration or fatigue.

A tailored density-based filtering strategy is offered to tackle this issue. Additionally, volume fraction is left unconstrained so material can be strategically replenished through a logarithmic rule acting on the updated compliance. In doing so, an interpolation space with three degrees of freedom (volume, compliance, minimum thickness) is created, yielding diverse topologies for the same boundary conditions and design values along different stages of evolving topological families with distinct features.

The optimization process is further accelerated by introducing the volume-compliance iterative scheme as a physical loss function in a Double Distance Neural Network (D²NN), obtaining similar results to 2,000 steps worth of vanilla iteration within 500 training epochs. This proposal offers a novel topology optimization design space based on minimum strut thickness - via filtering - and topological families defined by minimum volume fraction and compliance. The methodology is tested on several examples with diverse loading and boundary conditions, obtaining similarly satisfactory results, and then boosted via Machine Learning, acting as a fast and cheap surrogate.

Keywords: Topology Optimization, Filtering, Manufacturability, Machine Learning, Constrained Optimization, Bone remodelling, Mechanostat

1. Introduction

Before the Industrial Revolution, vernacular structural design (housing and bridges) offered utilitarian feasible solutions where simplicity and resistance were equally valued. These designs often failed due to then unknown or under-studied phenomena such as buckling and fatigue, and were mostly oversized for their intended task.

Nowadays, structures for industrial applications must be sturdy enough to withstand service specifications (technical requirement) while using the minimum necessary material (economic constraint), reaching a compromise between both criteria. The search for the optimum is now mathematically defined, depending on measurable physical variables.

After briefly introducing the state of the art in this first section, the novelties will be presented alongside several illustrative examples: material density correction in Section 2, the proposed erosion filter in Section 3, the growth-based optimization approach in Section 4 and a particular application for vibration purposes in Section 5. Section 6 will cover some relevant case studies applying the suggested methodology. Section 7 offers a Machine Learning surrogate to accelerate the optimization process and Section 8 will offer some conclusions and proposals for future research lines.

1.1. Topology Optimization

Topology optimization (TO) is a widely established technique [33, 39, 6, 5] for structural design problems where mechanical requirements are subjected to material restrictions by creating a topological object (adding holes) from an initial isotropic bulk block, yielding a binary distribution (material/void).

Among different techniques, the Solid Isotropic Material with Penalization (SIMP) [39, 6] is arguably the most common, due to its simplicity. It consists of an iterative minimization of compliance $\mathbf{c} = \mathbf{u}^T \mathbf{K} \mathbf{u}$ (twice the strain energy Ψ , i.e. stiffness maximization) subjected to a target, fixed volume fraction v_f via Young's modulus decrease $\mathbf{E}_{t+1} = \mathbf{E}_0 \rho_t^p$, where ρ is the material's density (from 0 - void - to 1 - full -) and p is a penalization parameter.

Alas, most topology optimization methods (SIMP, ESO, OMP, etc.) [38] can produce theoretically optimized structures which are not easily manufactured or feasible, especially for additive manufacturing (AM): discontinuities, acute angles, fragile struts, etc. This compromises durability as well, since thin struts are more prone to deteriorate and ultimately break. Plus, they could buckle if they are slender enough. Often times, they appear as a result of load or boundary condition variability. On top of that, they do not actually contribute significantly to supporting the load, conversely adding to the compliance sought to be minimized.

To tackle these shortcomings, many filters address material density [8, 43, 28, 1]. They can avoid numerical limitations like checkerboard patterns and mesh-dependence and practical ones like resolution and continuity, with various penalization schemes [32]. Some of them revolve around erosion phenomena, i.e., scratching material off the structure's contour to get a clear void-material frontier, as in nature [34]. Their effects are usually global, targeting all the contour simultaneously instead of specific areas of interest along the iterative process (a sort of evolutionary design). This kind of density filters do in fact enhance manufacturability as they sharpen the void-material boundaries, although they still do not selectively target undesired ribs - a consequence of load variability [22].

Many tools have been suggested with manufacturability in mind, particularly after the rise of AM and its implicit multi-scalar challenges [29] (length, connectivity, self-support) and opportunities (e.g., tailored anisotropy for functionally-graded metamaterials [56]).

Such tools tackle visibility of inner/void regions (mainly in 3D prototypes) to avoid complicated printing paths [13] and create self-supporting structures [27] with minimum support material or smooth contouring to avoid notches and acute angles. Level-set [50, 48] and spline-based methods [42, 37] suit those very purposes.

Remeshing, subdivision and fitting are widespread post-processing steps [43]. These tools are often computationally costly and jeopardize the solution's optimality [29]. For that reason, many topology optimization methods embed manufacturing constraints as a part of the iterative process [26] within a constrained optimization framework [24]. Despite some drawbacks regarding reduced design space and generality [46], the possibilities are plentiful, e.g., auxetic metamaterial design [2]. Interestingly, if volume fraction is left unconstrained, other design parameters can come into play [10, 55, 14, 3, 25].

1.1.1. Current interpolation schemes

Traditional TO methods yield a binary material (black, $\rho = 1$) and void (white, $\rho = 0$) distribution. Intermediate states (gray, $0 < \rho < 1$) frequently need finer profiling strategies [15] to define actual limits for material distribution. Relaxation for intervals through power laws is a common solution in stress-based [53, 30] and stress-constrained TO [17, 10]. However, it presents several problems, such as stress singularity (addressed by [9]) and the existence of solutions depending upon the parametrization of such power laws. The latter issue can be solved via linear slope approximation [35] and/or intervals for sensitivity filters [24].

The use of confidence intervals calls for interpolation techniques. However, this cannot be done to material layouts directly (topologies), rather to their associated descriptive matrices (density or stiffness, for instance) as an array of scalars - avoiding singularities and mesh-dependence by non-local methods [23]. Different densities can also be interpreted as various materials with their particular properties [7, 54], allowing for a more accurate design by getting rid of artificial density penalization. If volume is left unconstrained, material variability is maximized [40].

1.2. The Carter-Hayes theory

The idea signing different materials to each density value is coherent with Ashby's law for material selection [4] - Equation 1) relating initial E_0 and current E Young's moduli through their associated initial ρ_0 and current ρ densities:

$$\frac{E}{E_0} = \left(\frac{\rho}{\rho_0} \right)^\gamma \quad (1)$$

where γ is an adiabatic proportionality parameter.

This empirical expression is coherent several studies on the human bone's mechanical behavior [12, 11, 41]. Although common in Engineering applications, the nominal Young's modulus E_0 and density ρ_0 are mere homogenized assumptions, not to be found in an actual material cell. For that reason, effective properties with physical meaning (like x_{Phys} in top88.m [1]) are preferred.

1.3. The mechanostat theory for density evolution

Wolff-Frost's mechanostat theory [52, 16] - translated into mechanics by Huiskes [21, 20] and Weinans [51] - dictates a linear relationship betwixt mass growth over time (expressed via density $\rho = m/v_f$ for a fixed volume fraction) and strain energy $\Psi = Ku^2/2$ through B as a mechanistic growth parameter (scalar), as in:

$$\frac{d\rho}{dt} = B \Psi \quad (2)$$

This experimental relationship describes bone remodelling, the biological process by which bone cells (osteocytes) are created (synthesized by osteoblasts) or destroyed (resorption by osteoclasts) according to their load-bearing needs (mechanical imperative) [19]. This explains bone tissue adaptation to injuries (fracture, implants), age (osteoporosis) and illnesses (osteogenesis imperfecta). Such rationale will be introduced as a computationally cheap embedded filtering strategy with no need for post-processing steps.

2. Formulation of the effective density correction

Analogously to the aforementioned mechanostat, the evolution of density and compliance will be intertwined in this proposal. For every target volume fraction, a different starting point applies, giving way to separated interpolation curves converging to a single point where the structure is entirely solid ($\rho = 1$). This is not allowed by equation 1, restricted to $(\rho = 0, E = 0)$ as a start. Thus, an effective density ρ_{ef} is defined as the logarithmic update of the real value ρ_{re} given by the mechanostat equation 2:

$$Ln[\rho_{ef}] = Ln[\rho_{re}] + Ln[d\rho_{re}] \quad (3)$$

Which can be rewritten as:

$$Ln[\rho_{ef}] = Ln[\rho_{re} d\rho_{re}] \quad (4)$$

Replacing the mechanostat equation 2 into equation 4:

$$\rho_{ef} = \rho_{re} B \Psi dt \quad (5)$$

Assuming the Ψ independent from density on the grounds of step discretization, it holds:

$$\frac{d\rho_{ef}}{d\rho_{re}} = \alpha \Psi \quad (6)$$

With $\alpha = B dt$

Using the Carter-Hayes equation 1 again:

$$\rho = \rho_0 \left(\frac{E}{E_0} \right)^{(1/\gamma)} \quad (7)$$

Which, derived with respect to stiffness, gives:

$$\frac{d\rho}{dE} = \frac{\rho_0 \gamma}{E_0} \left(\frac{E}{E_0} \right)^{(1/\gamma-1)} \quad (8)$$

For the particular case of $\gamma = 1$, as a simpler approach:

$$\frac{d\rho}{\rho_0} = \frac{dE}{E_0} \quad (9)$$

For each initial volume fraction, the curves' respective ρ_0 and E_0 will be denoted as ρ and E from here onwards. The algorithm is now intended to optimize the strain energy density Ψ through variation of the local density ρ related to the Young's moduli E .

This inverse relationship is given by a constant ζ as $\Psi = \zeta/E$. Hence, the derivative of the Young's modulus with respect to the strain energy density yields:

$$\frac{dE}{d\Psi} = -\frac{\zeta}{\Psi^2} = -\frac{E}{\Psi} \quad (10)$$

The next step is to substitute the equation 10 into equation 9 to obtain:

$$\frac{d\rho}{\rho} = -\frac{d\Psi}{\Psi} \quad (11)$$

And using the $d\rho_{ef}$ instead of the real $d\rho$ (equation 6):

$$\alpha \frac{d\rho}{\rho} = -\frac{d\Psi}{\Psi^2} \quad (12)$$

Through the integration of both sides:

$$\alpha \ln[\rho] + \beta = \frac{1}{\Psi} \quad (13)$$

where β is the sum of the integration constants. Considering the equivalence $\Psi = 2c$ ($c = uKu$ being compliance) and $\rho = m/v$, the latter expression can be reshaped into:

$$\frac{1}{c} = a \ln(v) + b \quad (14)$$

where a and b are constants. More precisely, b corresponds to the lower limit of compliance c_{min} for a maximum volume fraction (and thus, stiffness), i.e. a domain filled with material and no void: $v_{max} = 1$. From the former equation, $b = 1/c_{min}$ can be obtained, in which c_{min} can be computed from simple analogy to the continuum.

Substituting b in Equation 14 yields a , a case-dependent constant defined by the initial volume fraction v_0 (considered of infinite compliance) and the minimum compliance c_{min} : $a = -\frac{1}{c_{min} \ln(v_0)}$. Substituting again in Equation 14, the resulting iterative scheme for volume fraction update is as follows:

$$v^{i+1} = \left(\frac{1}{c_{min}} - \frac{1}{c^i} \right) c_{min} \ln(v_0) \quad (15)$$

Having defined all constants and limits, Equation 15 describes the evolution curves of a given topology from the minimum to the maximum volume fractions while varying in compliance. Any data point along each of the curves represents an existing topology and thus allows for compliance-volume interpolation across different stages given by data points. These curves and the area below them constitute a constrained design dominion, offering an alternative to other more computationally expensive approaches [7, 45, 57].

This way, multiple volume fractions can provide different compliances and viceversa, on the designer's demand. If volume fraction is left unconstrained, compliance can be an objective on its own [10, 55] to generate compliant mechanisms [14, 3, 25]. Under this approach, the two most important parameters in SIMP (compliance c as the objective, volume fraction v as a restriction) are directly linked, simplifying the process as one unified expression updates both simultaneously where volume becomes a temporary constraint.

This formulation is coherent with some instances of logarithmic growth in nature, such as cell reproduction or virus propagation [47].

3. The erosion filter

To alleviate the concerns derived from feeble ribs in topology optimization (buckling, stress concentration, fracture, manufacturability), an additional filter is proposed in this article, besides the sensitivity and density ones already provided by [1]. As an erosion filter, this algorithm searches for neighboring elements with densities below a certain (user-defined) threshold within a given radius r and sets them to void, thus eliminating the unwanted twigs on a minimum-thickness basis. More precisely, it iterates through all non-void elements checking its neighbors at different distances horizontally, vertically and diagonally, in both senses, as in Figure 1.

Thus, if the advancement in opposite search directions exceeds the target diameter (for instance, $l_1 + l_5 \geq 2r$), the first adjacent elements encountered will be erased if their density is below the established threshold, that is, set to a negligible density value around 0.001 (non-zero to avoid singularity). Of course, the minimum resolution of this filter is that of the finite element mesh: 1 element. Assuming linear elasticity, scale is left to the user's interest.

This tool can be considered a minimum-thickness density filter, except its constant effects (applied with the same radius each X iterations) prevent mesh-dependence [43]. Other common manufacturability-oriented variables like minimum hole size and sharp edge avoidance are left unrestricted, since the evolution of the filtered topologies is expected to implicitly diminish their effects. The filter can be applied partially, direction-wise, if the user requires so.

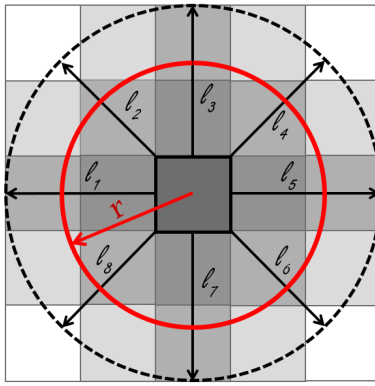


Figure 1: Filter with lengths $l_i, 1 < i < 8$ (black arrows) outside a radius r (red circle). Each element's color represents its physical density, ρ_{Phys} , from white (virtually void) to dark gray (full material).

After calling the new ad-hoc filter function *twigcutter.m*, the original physical density variable ρ_{Phys} is overwritten with the new filtered value $\rho_{Phys,filtered}$ containing the biphasic void/material distribution subject to a user's defined threshold (around 0.8 for the examples shown in this article). A minimum value is also enforced to avoid checkerboard patterns. This double filter enables local adaptation to manufacturing requirements.

As an illustrative example, let a 1000x200 cantilever beam be considered, fixed on its left-side wall and loaded with upward unit forces on both its upper and lower right corners. With *top88.m* [1] as a solver, its embedded density filter is applied with $r_{min} = 2$ (maximum feasible resolution, avoiding checkerboard patterns).

Algorithm 1 Logarithmic density correction and erosion filtering

Require: Setup of the model: boundary conditions and bounding volume.
Require: topological curve limits c_{min}, v_{max}
Require: logarithmic parameters a, b with Equation 14
Require: erosion filtering radius r
Ensure: FEA isotropic linear elastic calculation at $t = 0 \rightarrow K(^0E)U = P$ (top88.m [1])

- 1: **while** $change > tol$ and $v < v_f$ **do**
- 2: **Initialize** $\mathbf{c}, \mathbf{dc}, \mathbf{dv}, v_f = v_{min}$
- 3: **Update** v with Equation 15
- 4: **for** i in N_{loads} **do**
- 5: **Compute** K, sK (top88.m [1])
- 6: **Initialize** $(\mathbf{c}_i, \mathbf{dc}_i) = 0$
- 7: **Initialize** $\mathbf{dv}_i = 1$
- 8: **Filter** \mathbf{dc}_i (sensitivity) and \mathbf{dv}_i (density)
- 9: **Apply erosion filtering** (twigcutter.m) substituting ρ_{Phys} with $\rho_{Phys,filtered}$
- 10: **end for**
- 11: **end while**

Many thin ribs appear in the optimized topology - see Figure 2. This means the distribution of load will be quite heterogeneous: both the normalized shear strain (Figure 8b) and the von Mises equivalent stress (Figure 8c) are highly concentrated in junctions, cross-section changes and notches, which puts the structure at risk of fatigue failure (fracture). To get a simpler topology, the filter with radius $r = 5$ is applied in Figure 2.

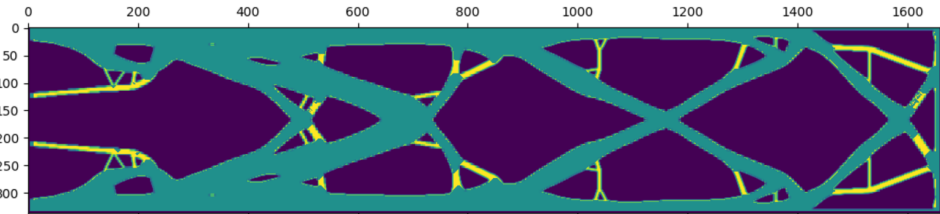


Figure 2: Filter of radius $r = 5$ applied to the a 1000x200 cantilever at iteration 1000 (Figure 8a). Dark blue represent void, yellow the erased (filtered) twigs and light blue the remaining structure.

The applied filter in Figure 2 effectively tackles most of those structurally superfluous yet difficult to manufacture twigs, which is among the main objectives. Alas, if such a trimming were to be directly introduced, it would not be structurally optimal either: many junctions would be left unsupported, discontinuities would further complicate manufacturing (needing supports if 3D-printed) and the target volume fraction would not be respected after getting rid of those elements.

Also, some junction points (joints) would be left with undesirable stumps unreachable by the filter as the distance to the main structure is greater than the prescribed radius r . Therefore, the filter must be embedded and applied not once at the end (post-processing) but periodically during the iterative optimization to allow for restructuring.

The filter cannot be enforced during the first iterations as the optimized structure is in its early growth stages, and so densities ρ_{Phys} have not yet reached values close to 1 (full), 0 (void) or any of the upper or lower thresholds to approximate both limits, mostly presenting an ill-defined intermediate density distribution.

Thus, it would create incompatibilities with the sensitivity/density filters in [1] or even force the full annihilation (void) of the emerging optimized topology, since no existing element's density would reach the established threshold. Alas, choosing the starting iterative step could prove difficult as different loading states generate varied optimized topologies, each of them with their own complexity and time (iterations) to converge.

A side effect of the filtering strategy is that of the decreased volume fraction, which could be leveraged as savings in material. Since the trimming operation takes an unforeseen amount of volume each time, the algorithm needs time to replenish the lost fraction to attain the target. However, if the iteration interval between prunings is too short, the topology might not have the chance to reach the desired volume fraction until no more twigs under the filtering radius are forming, which could take long. Thus, the timing of the filter is also a tuneable parameter. The interval (each X iterations) must be small enough to avoid unwanted regrowth but at the same time sufficiently big so as not to thwart the natural course of topology evolution.

Other option would be leaving volume fraction unrestrained along the iterative process, as proposed in the previous section. To reconstruct a more robust topology after the filter is applied, volume fraction must grow quasi-monotonically - as in equation 15 -, compensating the filter's momentary descent. Otherwise, the filtered structure would be even further restrained and the optimization process would be halted as the only possible change would be continuous retraction of material till total annihilation (full void domain). The practical implementation of the logarithmic densification (Equation 14) and the proposed erosion filter can be seen in Algorithm 1.

4. New optimization strategy using the growth space

We propose to distinguish between 3 design spaces for topology optimization designs, depending on the input data and expected outcomes, characterized by four main variables described η (set of boundary conditions), ρ (density of the design), α (final topology of the solution), and Ψ (strain energy).

With this we can define three spaces according to the optimized designs in the literature. Traditional TO is done in the $\Phi(\eta, \rho)$ space, with density and boundary conditions as inputs. In this paper, we propose the design space $\Gamma(\eta, \rho, \Psi, \alpha)$, where we can also impose the desired strain energy of the final structure. We see in figure 3 that a point in the Γ space can be reached through different topologies. It gives us insight about a richer space $\Lambda(\eta, \rho, \Psi)$ that also depends on the topology α , which can be prescribed as well. In this work, we present results on the Γ space.

This distinction between design spaces is relevant, since any point identified in Φ by its boundary conditions η and volume (density) fraction ρ could be associated with many strain energy states Ψ in Λ , which in turn correspond to a myriad of possible topologies α in Γ . This surjection is exemplified in Figure 3: in the Φ and Λ spaces the top and bottom results are exactly the same point, since both have the same volume fraction and strain energy. The only variation occurs in the Γ space due to the different topology α of both results.

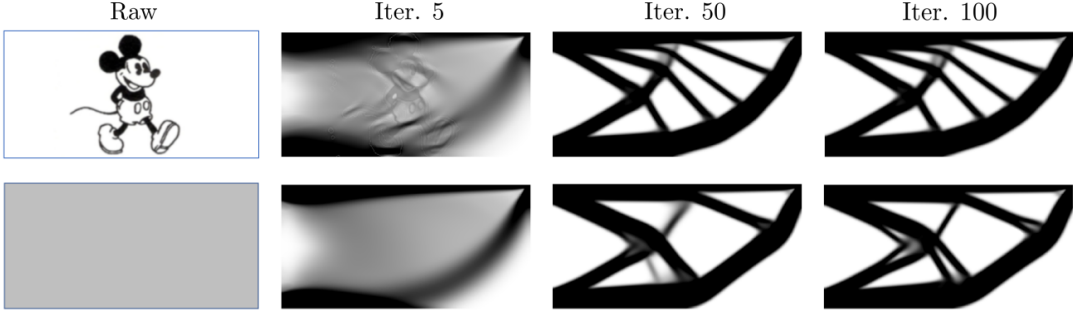


Figure 3: Topology optimization processes (rows) for a cantilever beam with different starting points: a randomly convoluted topology α (top) and the usual intermediate density block ($\rho = 0.5$, bottom). The same iterations (column-wise) share their boundary conditions η , volume fraction ρ and strain energy Ψ .

However, the starting point for the optimization process is not the only nuance to be considered. Through the proposed logarithmic densification (Equation 14), it is possible to reach equivalent points in $\Phi(\eta, \rho)$ yielding very different strain energies Ψ in Λ stemming from distinct starting points. See Figure 4 for an illustration: since each logarithmic curve designates a different iterative evolution, distinct topologies are expected for the same vertical (density) line as well (designs $A-C-E$ for $\rho = 0.3$ and $B-D-F$ for $\rho = 0.6$).

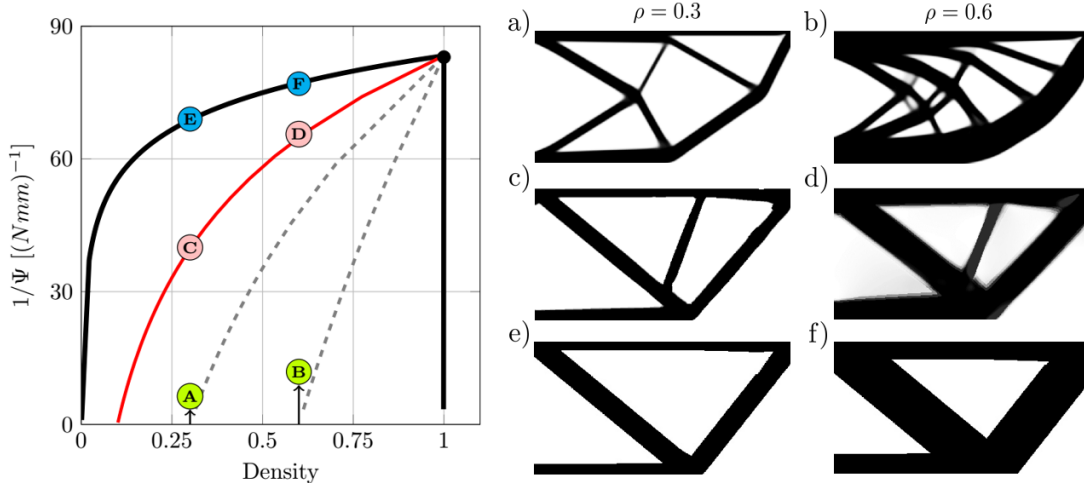


Figure 4: Different optimized cantilever beams (right) with column-wise equal densities ρ represented in the Λ space (left). Comparison between SIMP (green dots at the end of vertical arrows) and the proposed logarithmic densification starting from quasi-void (blue dots on the left-side black thick curve) and a very low density ($\rho_0 = 0.1$, pink dots on the red curve).

Whereas points A and B in Figure 4 are the result of regular fixed-volume compliance minimization (SIMP: convergence is given by a tolerance between iterations), points $C-D$ and $D-F$ are obtained via Equation 14, effectively dilating [44] an initial canonical topology: D and F are just thicker versions of C and E , respectively. For instance, following the curve corresponding to the initial density for topology A , its logarithmic evolution is displayed in Figure 5 by dilation of said starting point (a). This examples demonstrate Λ space's greater versatility when compared to Φ .

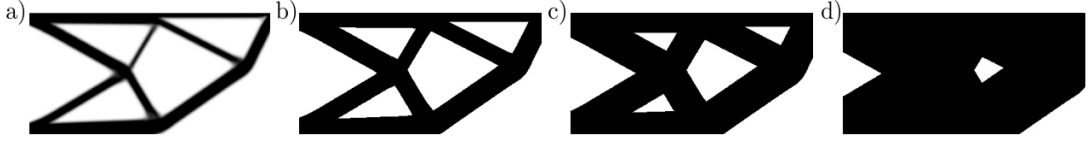


Figure 5: Topological dilation on the $\rho_0 = 0.3$ curve from Figure 4. Other examples can be found in Figures 12 and 15.

The variety of material layout choices available in Λ for the very same volume fraction (unobtainable through plain SIMP) has mechanical implications as well. Consider the von Mises stress fields for A , B and C (from Figure 4) in Figure 6: the topological simplification in the proposed designs C and E simpler (w.r.t. A , in increasing order) is due to the strengthening and/or disappearance of thin ribs responsible for most of the topology's deformation (and so, compliance) - which can be further reinforced through the proposed erosion filter. This makes the structure stiffer, demonstrated by the lower stress concentration.

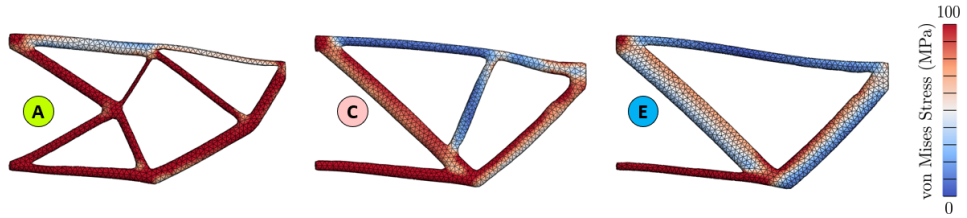


Figure 6: Von Mises stress comparison for topologies A , C and E in Figure 4.

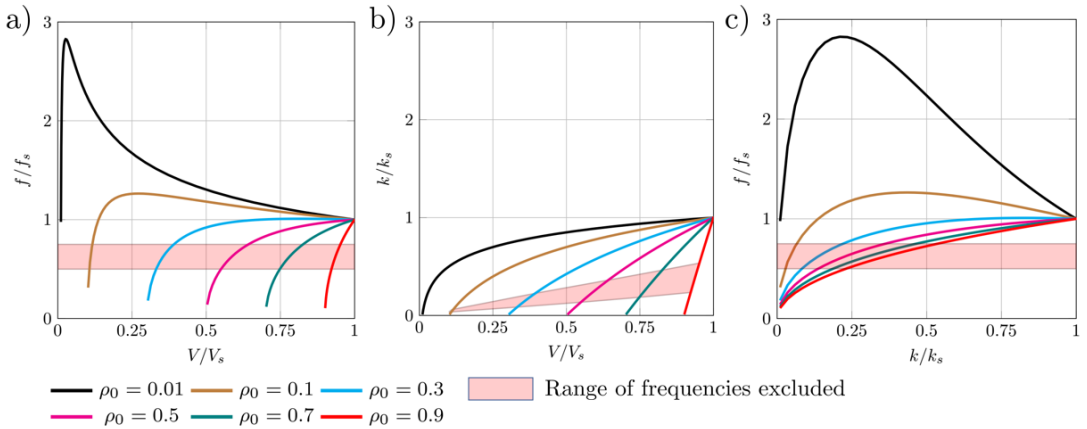


Figure 7: Normalized design curves (w.r.t. solid block values) for volume-frequency (a), volume-stiffness (b) and stiffness-frequency (c) for several initial densities ρ_0 , showcasing a band-gap in red.

5. Design for a target natural frequency

For a sole isotropic material, i.e. SIMP's assumptions, parameters ρ and Ψ within the Λ design space are tantamount to mass m and stiffness k , respectively - allowing to compute the prototype's natural frequency f_0 :

$$f_0 = \frac{1}{2\pi} \sqrt{\frac{k}{m}} \quad (16)$$

This offers many direct applications in Engineering, such as vibration prevention or acoustic resonator design [49] - a common goal for metamaterials. Although SIMP is by default designed to maximize stiffness, the regular approach [6] does not allow for volume (or density) tailoring and yields artificial frequency modes when low-density cells are penalized. Hence the use of genetic/evolutionary methods by some authors [36, 18], where volume is unconstrained.

The iterative scheme suggested in this article (Equation 15) permits flexible volumes and frequency control without solving costly eigenvalue problems [31]. For instance, to select (or avoid) a frequency value or range, it suffices to visualize the frequency/stiffness/volume interval and its intersections with predefined topological curves and select iterative parameters ρ_0 , ρ_i , v_i accordingly. See Figure 7 for an example.

6. Results

In this section, the proposed tools (volume-compliance interpolation, erosion filtering and their respective and combined applications) will be put to the test on several practical case studies.

6.1. Filtering radius in topology optimization

The filtering algorithm *twigcutter.m* will be called every 10 iterations, considering it a lapse long enough to polish the protruding remains while short enough to impede any pernicious regrowth of the freshly cut parts. To avoid further constriction of the design space, the volume fraction grows constantly by a fixed amount starting from an initial prescribed value (about 90% of the target) until the target fraction is met.

This way, the structure has room to regrow structurally meaningful ribs while obtaining the desired target as the twigs are periodically severed. Sometimes, the eliminated volume is greater than what can be regenerated within the filtering interval, so the volume fraction is somewhat lower than the desired target - which could be construed as an additional advantage, since material efficiency is further ensured.

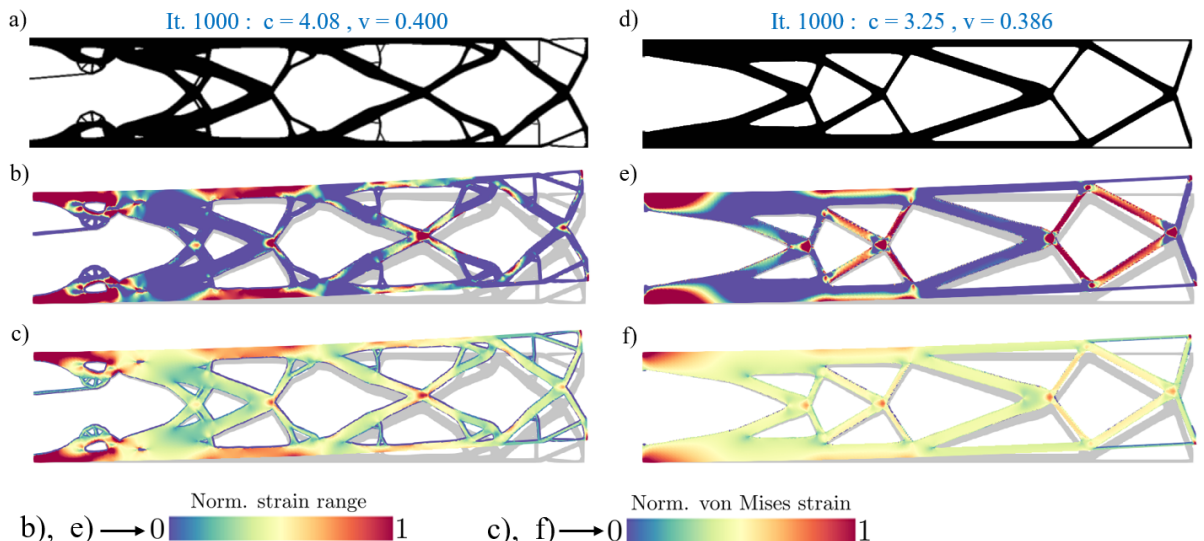


Figure 8: Vanilla (left) and filtered (right) topology optimization of a cantilever beam with upward loads in both right corners, iteration 1000. The resulting optimized structures (a, d) are shown along their shear strain and von Mises equivalent stress distributions (b,c and e,f respectively).

The topologies obtained after 1000 iterations are showcased in Figure 8, with their respective normalized shear strain and equivalent von Mises stress (b and c for the unfiltered version (a), e and f for the filtered one (d)). Focusing on the left side (Figure 8a, b and c), it is easy to notice how the thinnest struts are not actually performing any strain or stress transfer worth of mention in the vanilla topology - especially regarding shear strains since loading is vertically applied -, rendering them useless. As a result, both shear and strain are highly concentrated in some joints and near loading points and supports, whereas the remainder of the structure is idle, supporting a fraction of the load.

The filtered version (see Figure 8d) is noticeably simpler and sturdier: the genus, i.e., “number of holes”, has decreased greatly and the majority of those inconvenient twigs have disappeared giving way to thicker, more robust ones with a meaningful contribution to load bearing - namely between joints and support points. Additionally, the stumps seen in Figure 2 have been completely erased as a result of the iterative process.

This has noticeable effects on their shear strain (Figure 8, second row) and von Mises equivalent stress (Figure 8, third row): having fewer struts guarantees a more consistent and homogeneous load distribution, so that a smaller set of ribs are structurally meaningful, instead of unevenly loaded sections of struts which create unnecessary and dangerous stress concentrations. This is preferable both from a mechanical and a practical point of view (manufacturability), since reinforcing those individual struts entirely (e.g., making it thicker or choosing a sturdier material) is easier than doing so with multiple local points.

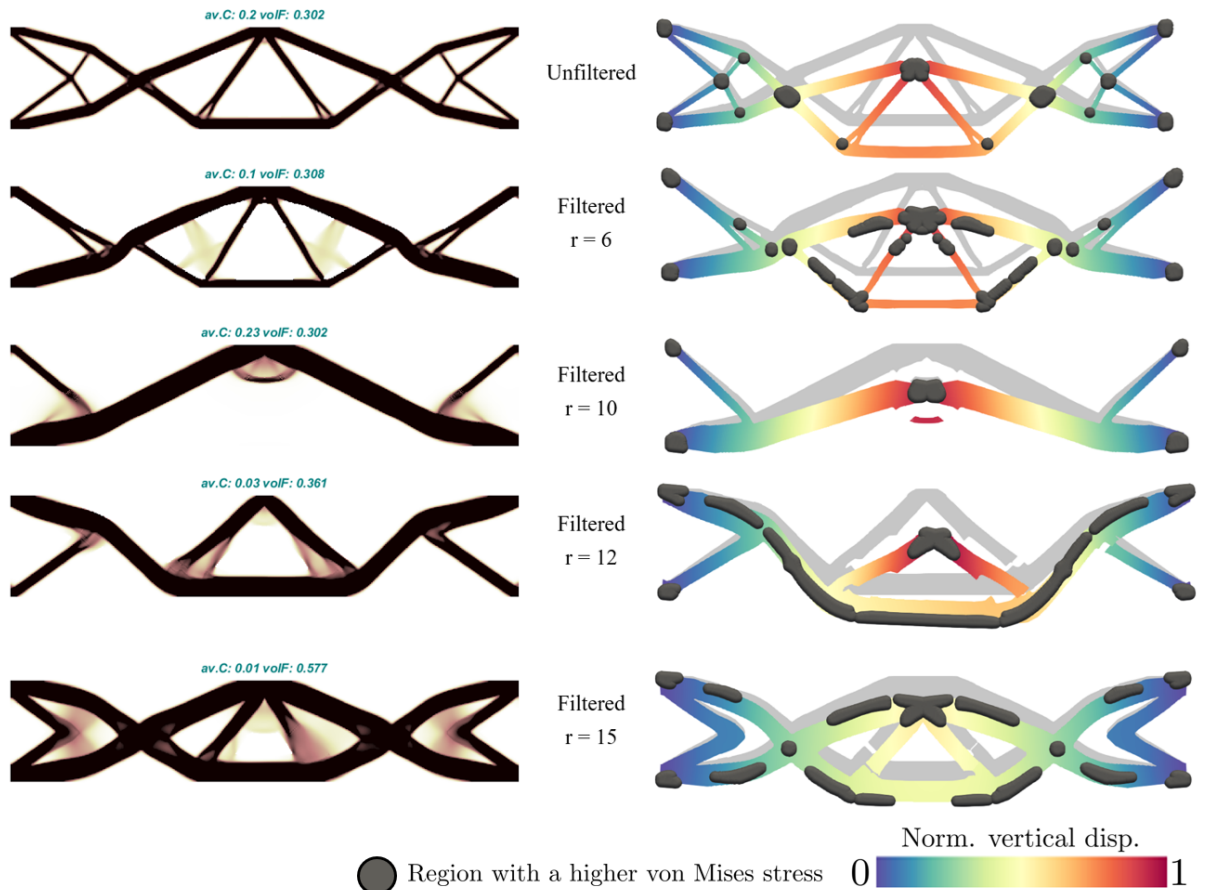


Figure 9: Optimized topologies for a beam fixed on both ends under a unitary downward load in the middle upper section (left) with their respective vertical displacement (color map) and von Mises (over 0.05 MPa in gray) equivalent stresses on the right: unfiltered (1^{st} row), $r = 6$ (2^{nd} row), $r = 10$ (3^{rd} row), $r = 12$ (4^{th} row), $r = 15$ (5^{th} row).

Interestingly, zero-shear areas (in blue, second row in Figure 8) imply equal principal stresses ($\varepsilon_1 = \varepsilon_2$), which could be further leveraged for manufacturing purposes, e.g. by printing filaments along those principal directions so strength is maximal.

On top of the mechanical improvement, computation power is also well administered: since the trimming process is done at the same time as the regular topology optimization, it does not imply any noticeable additional computational power, being run on a single core i7 1.8 GHz, 16 GB RAM in about 1.5h time till iteration 1000.

The filter is suitable for any applied loads and boundary conditions. For instance, a double-fixed beam with a single unitary downward load is subjected to filtered topology optimization with various radii, whose results can be seen in Figure 9. As expected, topologies get simpler on the filtered cases, although not always monotonically with an increasing radius, since boundary conditions still play an important role.

As the radius grows, two mutually linked effects are noticeable (see Figure 9 left, on top of each topology): volume fraction grows and compliance decreases (that is, stiffness increases). The former is expected, considering the algorithm needs to restock structurally important ribs in an ever-thicker version to comply with filtering requirements, which in turn provokes compliance descent: topologies become simpler (fewer deformable parts) and stiffer (less deformation overall). This can be clearly seen in their respective vertical displacement color maps in Figure 9 right.

As hinted before, von Mises equivalent stress (highest values in grey in Figure 9 right) is homogenized in filtered versions: continuous areas along most structurally relevant struts as opposed to local points in junctions and supports in unfiltered equivalents. Density in filtered topologies is less sharply defined than in its unfiltered counterpart (Figure 9 first row), even less so for greater radii. This boils down to the need to recover greater volumes scrapped off by the filter, which takes longer if the trimmed fraction is bigger, so convergence to the underlying optimal topology is slower.

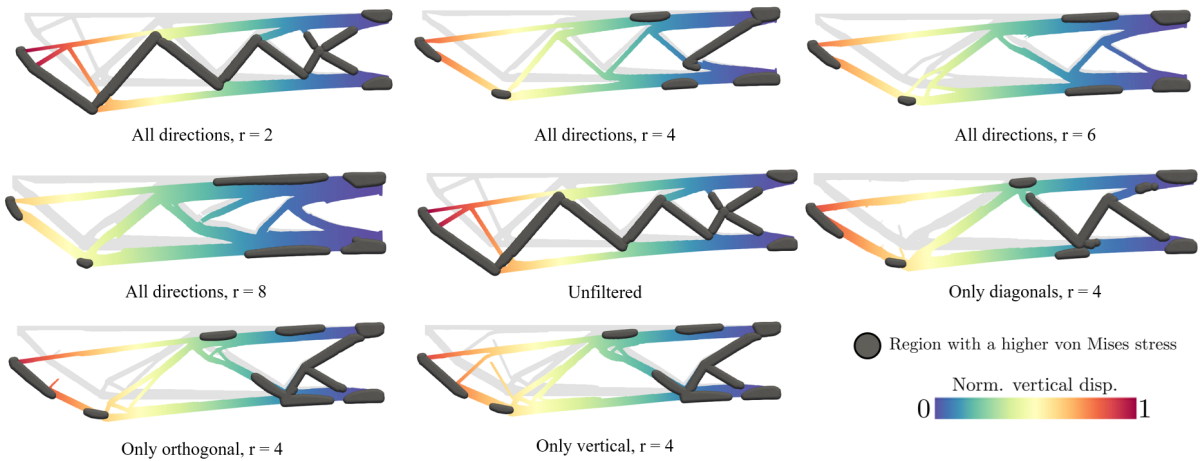


Figure 10: Displacement (color scale) and von Mises stress (over 0.05 MPa in gray) for different optimized cantilever beams (downward unit force on the upper left corner) under erosion filtering.

The filter can also be applied partially, i.e. exclusively in some search directions. See Figure 10 for a cantilever example. Again, filtering effects are easier to see when the radius is high: while there's virtually no difference for lower radii (compare *Unfiltered* and *All, r = 2*, for instance), heavier filtering creates simpler topologies with more homogeneous displacement (color map) and stress (gray areas); overall stiffer (notice the smallest tip displacement for the biggest filtering radius, $r = 8$).

However, asymmetric filtering can yield different results. Diagonally applied filters favor diagonal struts, longer in the center section and mostly stressed near the support and loading point (see 9 center right for $r = 4$ and directions 135° and 315° , that is, l_2 and l_6 in Figure 1). Orthogonality (directions l_1 , l_3 , l_5 and l_7 in Figure 1) offers further ramification in the remaining unfiltered directions (diagonals) and more localized stresses. If the filter is just applied vertically (directions l_3 and l_7 in Figure 1), horizontal capillarity is allowed and thus some ribs are closed.

This partial filtering could prove useful to induce tailored anisotropy for mechanical reasons (e.g. printing directions), thus controlling the incidence of buckling, compression, traction, etc. to meet the designer's requirements (material, boundary conditions, reliability, manufacturing method).

6.2. Structural designs within the growth space

An example of logarithmic optimization of a 3-point bending beam with downward unit forces applied in half length with different volume fractions and compliances can be seen in Figure 11, as a result of several independent optimization processes starting on different minimum volumes $v_0 = 0.1$, $v_0 = 0.3$, $v_0 = 0.5$ and $v_0 = 0.7$. The detailed information for data points *a-f* is contained in Table 1.

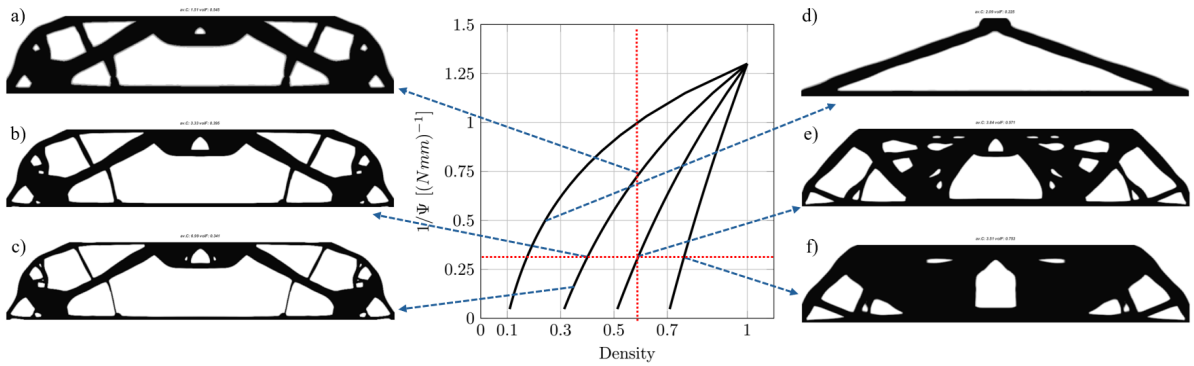


Figure 11: Unfiltered evolving topologies for a 3-point bending structure and several initial volume fractions: 0.1 (left), 0.3 (middle left), 0.5 (middle right) and 0.7 (right).

Fig. 7	a	b	c	d	e	f
v_0	0.3	0.3	0.3	0.1	0.5	0.7
v_i	0.545	0.395	0.341	0.225	0.571	0.753
c_i	1.51	3.33	6.99	2.09	3.84	3.51
i	65	45	25	125	20	15

Table 1: Information associated to topologies shown in Figure 11: initial v_0 , and current volume fraction v_i and compliance c_i for iteration i (3-point bending).

Focusing on Figure 11's left side, the development of a topological family with $v_0 = 0.3$ can be seen at different iterations: 25 (c), 45 (b) and 65 (a). Since the filter has not been applied, the only possible way to grow in volume is widening the already existing ribs, which in turn lowers compliance (structures get stiffer). This approach resembles plain shape optimization, where topology remains practically invariant (aside from little holes being engulfed by strut thickening alone).

If the designer is aiming at lower volume fractions, the optimized topologies get much simpler (triangular, linking loading points and supports directly) and relatively stiff, although they take longer to converge since the initial volume is too low to evolve into low-compliance structures too soon. See Figure 11d (starting volume $v_0 = 0.1$) for an example with $v_i = 0.225$ and $c_i = 2.09$ at iteration $i = 125$ (Table 1).

Should the modeler want stiffer options, starting with higher volume fractions could help speed up convergence to a desired compliance. Consider labels b , e and f in Figure 11 and their respective data in Table 1: while all three topologies have approximately the same compliance c_i , their respective volume fractions v_i are very different (f 's being almost twice as big as b 's), and their time to convergence is too (b takes three times as many iterations i to generate compared to f).

Thus, v_0 becomes a key user-defined hyper-parameter controlling both computation time (number of iterations) and final volume fraction v_i for a given compliance c_i . The needs of each topology will be determined by the material and boundary conditions. Interestingly, isochoric (vertical) lines, like the one (approximately) linking topologies a and e , represent processes with variation of compliance for the same volume.

Note that moving upwards in Figure 11 means lowering compliance while maintaining volume fraction, i.e. the regular SIMP method. Going downwards is also possible if the goal is a more compliant structure, among many other strategies neglected by SIMP.

This way, design interpolation would be possible by jumping between different logarithmic curves (with their respective v_0). Transition between curves can be done horizontally (fixing a compliance limit c_t and varying the volume fraction v_i till intersection with the desired volume curve) or vertically (fixing a volume threshold v_t and adjusting the compliance c_i until the objective curve is reached). See Figure 12 for some examples of interpolation (filtered/unfiltered, horizontal/vertical).

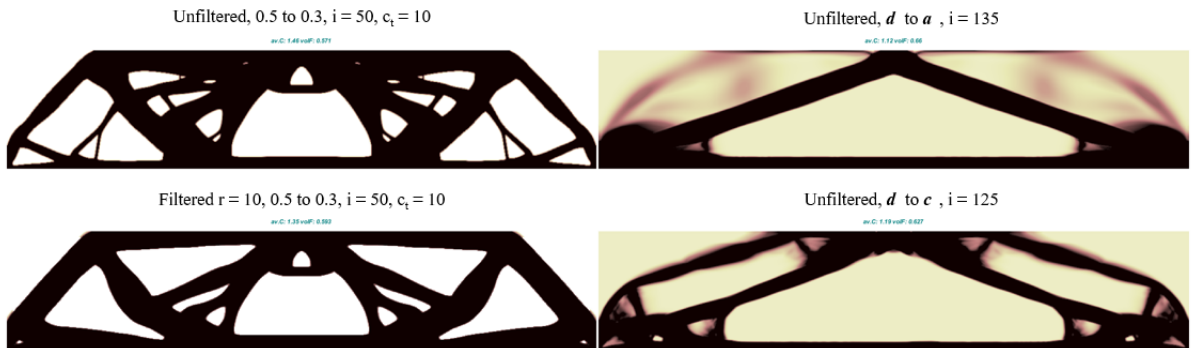


Figure 12: Hybrid topologies generated by interpolation between different v_0 curves: mixed 0.3-0.5 topology at iteration 50 with (lower left) and without $r = 10$ filter (upper left) with a compliance threshold of $c_t = 10$ and $v_0 = 0.3$ curves and volume-threshold interpolation between d and a (upper right) and between d and c (lower right).

On Figure 12's left side, some examples of horizontal interpolation (compliance threshold $c_t = 10$) are displayed. Both topologies closely resemble the initial curve's family ($v_0 = 0.5$, e.g. Figure 11e). For the same iteration ($i = 50$), the filtered case ($r = 10$, lower left) yields a simpler material layout than the unfiltered case (upper left), a “cleaner” structure with equivalent mechanical properties: similar compliance (up 1.46 vs down 1.35) and volumes (up 0.571 vs down 0.593). An exact match could be found if needed.

Figure 12 right (vertical interpolation with volume threshold v_t) showcases the importance of both the initial curve (determined by its initial volume fraction v_0) and the amount of iterations on each curve: while the resulting topologies do reflect aspects of both curves, the initial one ($v_0 = 0.1$) clearly prevails, judging by the absence of central vertical ribs (present in both *a* and *c*) under the load-support triangle (coming from *d*).

Thus, path-dependence applies to this kind of interpolation schemes, and so it must be taken into account accordingly. These intermediate solutions remain close in compliance (up 1.12 vs down 1.19) and somewhat in volume (up 0.660 vs down 0.627). Reaching the exact targets (Figures 11a and 11c, respectively) becomes difficult due to the many factors involved (initial volume, interpolation, threshold, boundary conditions, filters, etc.). Importantly, volume fraction (and thus, density) can only be fixed or increased ($v_{i+1} \geq v_i$), since a decrease in volume contradicts Equation 15.

The obvious differences between horizontal (c_t) and vertical (v_t) interpolation are due to the chosen iterative scheme: according to Equation 15, the next iteration's volume fraction v^{i+1} is directly depending on the current iteration's (averaged) compliance c^i - an exclusive result of the undergoing SIMP optimization -. This implies that constant compliance interpolation (horizontal, Figure 12 left) does not incur in any meaningful volume changes (unless a filter is applied, see Figure 12 lower left). Hence, topologies remain more or less unchanged when compared to their initial curve's ($v_0 = 0.5$) canonical shape (same “topological family” as Figure 11e).

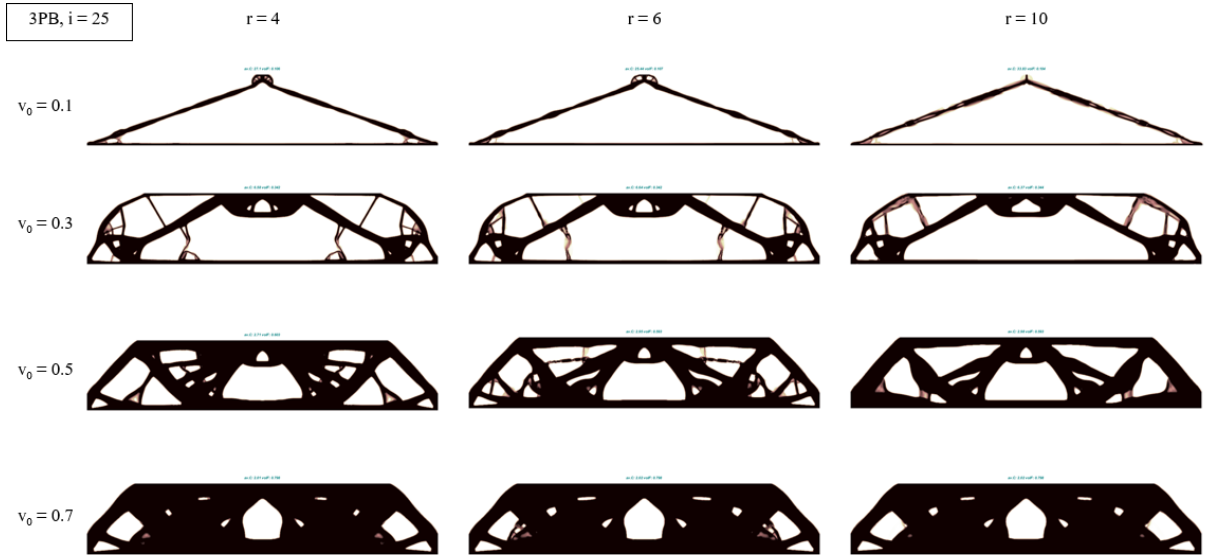


Figure 13: Filtered versions of the 3-point bending topology with different radii (4, 6 and 10) and starting volume fractions (0.1, 0.3, 0.5 and 0.7). Iteration 25.

$c_i v_i$ (i = 25)	r = 4	r = 6	r = 10
$v_0 = 0.1$	27.1 — 0.106	25.44 — 0.107	33.83 — 0.104
$v_0 = 0.3$	6.58 — 0.342	6.64 — 3.42	6.37 — 0.344
$v_0 = 0.5$	2.71 — 0.603	2.95 — 0.593	2.98 — 0.593
$v_0 = 0.7$	2.01 — 0.798	2.02 — 0.798	2.02 — 0.798

Table 2: Compliance c_i and volume fraction v_i for topologies shown in Figure 13.

Conversely, vertical interpolation (constant volume v_t , Figure 12 right) allows a free evolution of compliance between curves, so an intermediate trade-off solution is found between the beginning and ending “canonical topologies”, with a greater influence of the latter for already disclosed reasons. In these cases, convergence is slow and ill-defined. Interpolation between more than two curves would also be possible, although complex, needing enough iterations in between.

Leveraging both the filter and the logarithmic approach, very diverse topologies can be obtained for the very same design requirements (compliance, volume fraction). Let the 3-point bending beam be considered again. Several starting volumes v_0 and filtering radii r are enforced to produce a plethora of design points with similar compliance c_i and volume fraction v_i but very different topologies.

Figure 13 and Table 2 show an array of topologies for iteration $i = 25$ and various starting volumes v_0 (0.1, 0.3, 0.5, 0.7) and filtering radii r (4, 6, 10), with their respective compliances c_i and volume fractions v_i .

Row-wise, greater filtering radii (rightwards) “simplify” the topologies, reducing their *genus* (“number of holes”), as observed in previous examples. Column-wise, bigger starting volume fractions v_0 (downwards) densify the structures, performing a sort of shape optimization (as in Figure 11c to a) while significantly altering their genus.

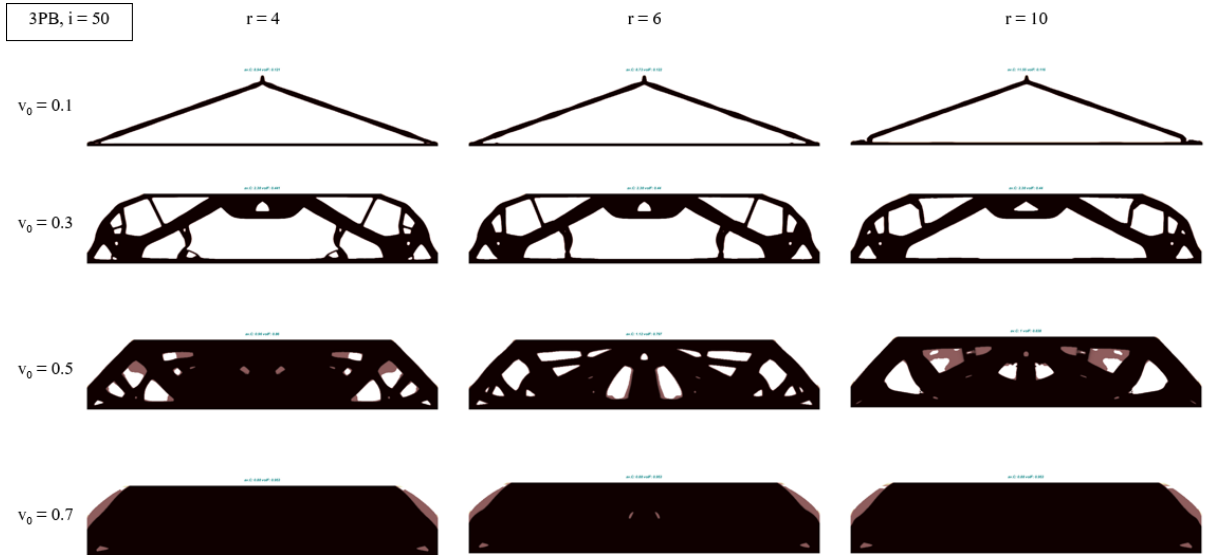


Figure 14: Filtered versions of the 3-point bending topology with different radii (4, 6 and 10) and starting volume fractions (0.1, 0.3, 0.5 and 0.7). Iteration 50.

$c_i v_i$ ($i = 50$)	$r = 4$	$r = 6$	$r = 10$
$v_0 = 0.1$	8.94 — 0.121	8.73 — 0.122	11.55 — 0.116
$v_0 = 0.3$	2.38 — 0.441	2.38 — 0.440	2.38 — 0.440
$v_0 = 0.5$	0.96 — 0.86	1.12 — 0.797	1.00 — 0.838
$v_0 = 0.7$	0.88 — 0.953	0.88 — 0.953	0.88 — 0.953

Table 3: Compliances c_i and volume fractions v_i for topologies shown in Figure 14.

According to Table 2, topologies in the same row (same v_0 , different r) present very similar volume fractions v_i . This is expected, since they are contained in the same v_0 curve under the same number of iterations i .

Such is the case of their compliances (c_i), thus representing different topologies for virtually the same data point (v_i, c_i) in Figure 11 - which offers an unmatched design flexibility. This row-wise equivalence is truer the closer radii are to each other and the greater the starting volume fractions are, where the design space is more constrained and coincidence is almost exact.

For very low starting volumes (e.g., $v_0 = 0.1$), their simpler topology is far less limited and so distinct features for each filtering radius provoke relatively important fluctuations (see middle top on the topologies shown in Figure 13 first row) in volume and, most importantly, in compliance. Nevertheless, these discrepancies can be solved by slightly varying iterations, since it has been mentioned that convergence follows different paces depending on the chosen logarithmic curve and filtering strategy.

Observing Figure 14 and Table 14 for iteration 50, some of the topologies seen in Figure 13 have noticeably evolved (middle volumes, namely $v_0 = 0.3$ and $v_0 = 0.5$), while others remain practically unaltered (lower volume, $v_0 = 0.1$). Higher volumes ($v_0 = 0.7$) have almost reached the maximum possible stiffness (highest volume, lowest compliance), i.e. the full material block. Table 3 reflects closer compliance and volume values for the same row than Table 2, virtually identical for $v_0 = 0.3$ and $v_0 = 0.7$.

All the remarks and observations applied for this case of study remain true for different loads, boundary conditions, radii and starting volumes, as soon as linear elasticity is kept. The combination of both tools presented in this article (filtering and logarithmic densification) provides a powerful and versatile inverse design methodology with three degrees of freedom: compliance c_i , volume fraction v_i and filtering radius r (somewhat equivalent to minimum thickness).

7. D²NN interpolation with effective density correction

This example is designed to implement a Double Distance Neural Network (D²NN) with Equation 15 as a physical loss function evaluating how far is the evaluated data point from the corresponding logarithmic curve, as well as the distance within.

Algorithm 2 D²NN interpolation

Require: Setup of the model: boundary conditions η and bounding volume ρ .
Require: topological curve limits c_{min}, v_{max}
Require: logarithmic parameters a, b with Equation 14
Require: erosion filtering radius r
Ensure: FEA isotropic linear elastic calculation at $t = 0 \rightarrow K(^0E)U = P$ (top88.m [1])

- 1: **Define** function *resize image* to scale image resolution
- 2: **Define** function *load data* for c, v and topology image files
- 3: **Define** class *D²NN* featuring a sequential architecture and forward propagation
- 4: **Define** function *D²NN loss* with Equation 15.
- 5: **Define** function *D²NN training* applying the *adam* optimizer for N epochs
- 6: **Define** function *generate image* from c, v targets
- 7: **Define** function *save image*
- 8: **Call** function *load data* upon the (c, v, image) dataset
- 9: **Call** function *D²NN training* to train the *D²NN* model with the loaded dataset
- 10: **Set** design targets c_t, v_t
- 11: **Call** function *generate image* upon the design targets c_t, v_t
- 12: **Call** function *save image* upon the new output image

Therefore, an interpolation framework is created to efficiently define topologically optimized structures with a given volume fraction and strain energy within a design space $\Lambda(\eta, \rho, \Psi)$, bypassing the need for relaxation methods or multi-material combinations and their inherent computation complexity.

A D²NN-driven surrogate is devised to accelerate TO convergence, featuring alternating linear (3) and ReLU layers (2) and a final sigmoid pooling. The model is trained for 500 epochs to predict compliance and volume values from topologies as image files, as in Algorithm 2. A 600x200 cantilever beam is considered for a case study.

A 20-point dataset is fed to the D²NN model, half of them generated with $r = 1$ (Figure 15 and the other half with $r = 1$ (Figure 16). Each set of 10 points is denoted with letters *a-j* in Figure 17 showcasing curves for different initial volume fractions along which data points P1, P2, P3 and P4 are located. Whereas P1 and P2 are within the training dataset, P3 and P4 are external to it. The points *d* and *e* are also used for an example of interpolation within a curve.

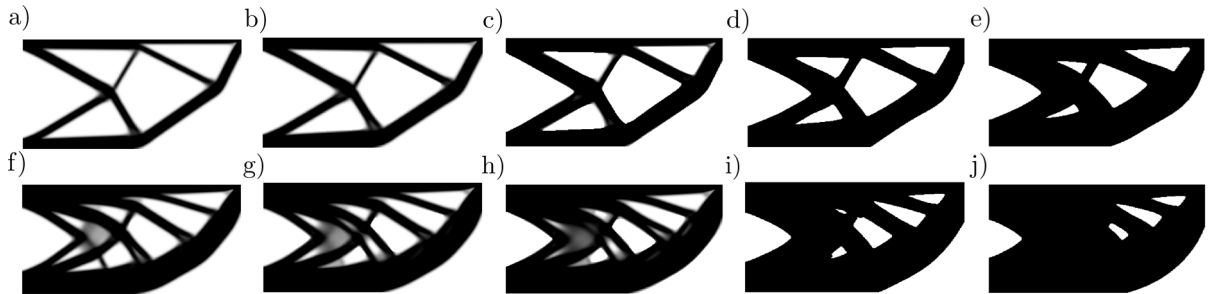


Figure 15: Training set: points A-J in Figure 17 for the ML surrogate with filtering radius $r = 1$.

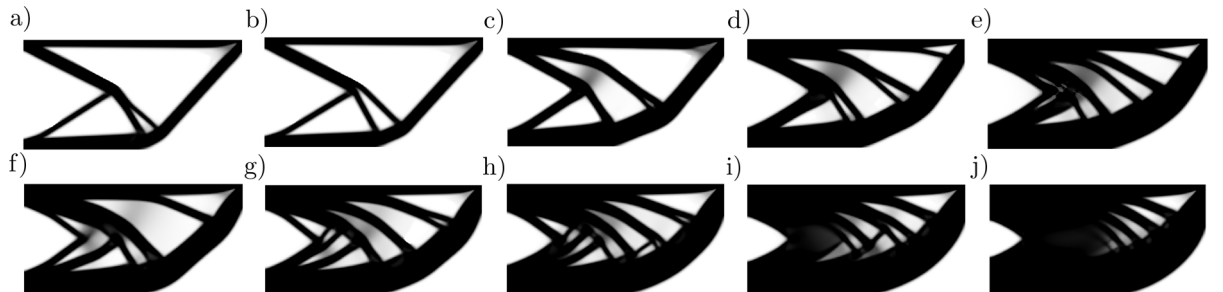


Figure 16: Training set: points A-J in Figure 17 for the ML surrogate with filtering radius $r = 4$.

These images depict interpolation points A-J in Figure 17, serving as database to obtain intermediate topologies P_1-P_4 via Equation 15, D²NN or both - see Figure 18. The physical loss in the D²NN scheme is given by the distance (in compliance and volume) between the interpolation point's and the target's respective curves.

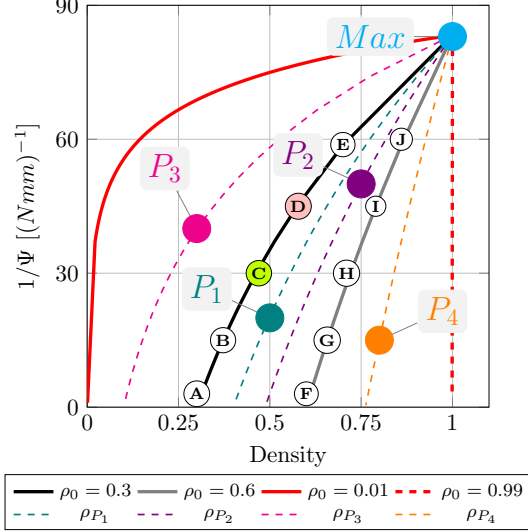


Figure 17: Evolution of inverse strain energy $1/\Psi$ over density ρ given by Equation 13 for several starting volume fractions v_0 .

The results of training the D²NN model with Figures 15 and 16 and testing it on unseen data points P_1 - P_4 in Figure 17 is displayed in Figure 18, using FEBIO© as a visualization tool and representing von Mises stress on stainless steel prototypes (AISI 316L, $E = 193$ GPa, $\nu = 0.33$).

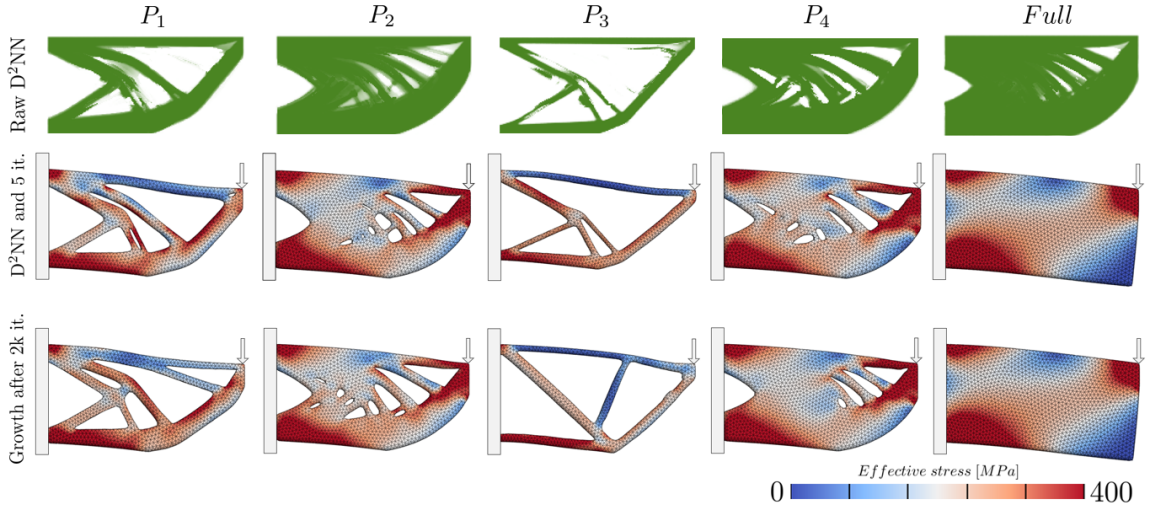


Figure 18: Topology optimization of a cantilever beam for points P_1 - P_4 and the full material block (columns), via D²NN exclusively (top row), D²NN after 5 initial iterations of Equation 15 (middle row) and 2,000 iterations (bottom row). Blue-red scale indicates stress values (MPa). Erosion filtering radius $r = 4$.

Figure 18 exhibits great column-wise similarities, meaning the D²NN-based surrogate (500 training epochs, top row) reaches very close results to the vanilla scheme (2,000 iterations, bottom row), saving a lot of computation time since, once trained, the D²NN-driven option is about 25 times faster.

If the D²NN scheme is only run for its 5 first iterations (middle row) rather than doing so from the initial curve's volume v_0 , the results when applying Equation 15 on the predicted ρ are even closer to the ground truth, with almost exactly matching stress distributions - especially in the full configuration.

Of course, this resemblance is never exact, since the dataset (A-J) is made up from points in different curves than the targets P_1-P_4 - see Figures 15 and 16 for examples with filtering radii $r = 1$ and $r = 4$, respectively, excluding the full volume block as the convergence point of all curves. Thus, this methodology could be interpreted as a quick way to obtain mechanically equivalent designs to the target - in terms of compliance, volume and minimum thickness - without actually having to compute all the needed iterations along their unexplored curves.

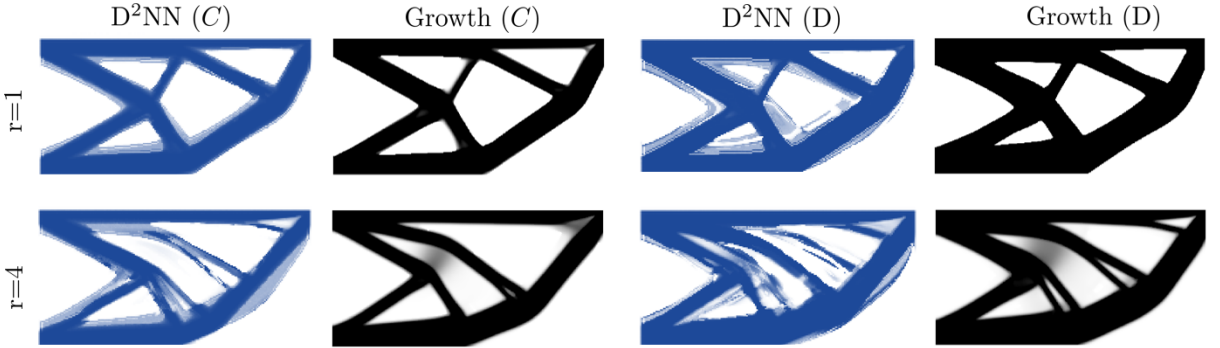


Figure 19: Data point ground truth (logarithmic growth with Equation 15, in black) and D^2NN prediction (in blue) along the training dataset curve A-E in Figure 17 (points C and D) for filtering radii $r = 1$ (top row) and $r = 4$ (bottom row).

This tool can also be employed to predict points along the same A-E and F-J curves, quickening dataset generation for training and so further accelerating the whole TO approximation process. See Figure 19 for some such examples: predictions are now much more accurate, since interpolation is done along the same curve for datasets and targets. This disrupts SIMP's initial homogeneous assumption, accelerating convergence.

If D^2NN training is performed upon a reduced order dataset (e.g. via Singular Value Decomposition), the topology's resolution can be tuned to produce slightly different results with virtually equivalent mechanical properties at a lower computational cost. See Figure 20 for some examples of D^2NN -predicted (raw) and 45 iterations of Equation 15 for reduced eigenvalue sets, suitable for Principal Component Analysis.

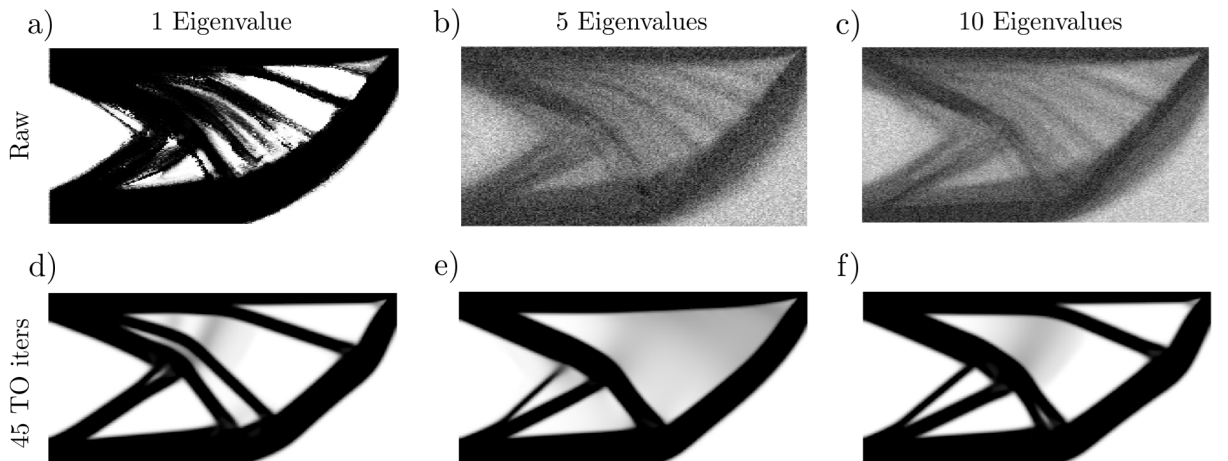


Figure 20: D^2NN forecasts (top row) and 45 logarithmic iterations (Equation 15, bottom row) with the first 1 (left column), 5 (middle column) and 10 eigenvalues (right column).

Columns in Figures 18 and 20 are instances of diverse topologies for the same volume fraction ρ and strain energy Ψ in the Λ space representing a sole $\Phi(\eta, \rho)$ point. As explained in Figure 3, this is but a consequence of the non-convex, highly non-linear solution space in TO, in which many initial points can lead to virtually equivalent designs in the Φ and/or Λ spaces, highlighting the need for a richer $\Gamma(\eta, \rho, \alpha)$ space able to tell topologies α apart.

8. Conclusions and future research lines

This article has introduced some shape and mechanical issues affecting most common topological optimization schemes, namely capillary struts which, although mathematically correct (following the minimization process), do not efficiently distribute neither material nor mechanical loading (strain/stress), making them prone to stress concentration and thus vulnerable to fracture, among other problems; apart from difficult to manufacture depending on the chosen technique.

Two novel approaches have been offered as ways to alleviate such drawbacks. The first one consists of a density filter which effectively eliminates those useless thin ribs while redistributing an equal or even smaller volume more wisely, which in turn improves mechanical performance. The second proposal consists of an analytical expression linking the two main design variables in the SIMP method (compliance and volume fraction) in an experimentally-consistent manner which in turn provides different “families” evolving in shape and topology. Importantly, these two ingredients can be combined and allow for interpolation, as seen in various examples, and introduced in a Machine Learning surrogate scheme.

These tools have been put to the test under various boundary conditions and loadings, proving they can create a versatile design space Λ with adjustable compliance c , volume fraction v and minimum thickness (via r); all of that within reasonable computational cost. This is deemed of great interest for practical reasons, since this article explains the full methodology for simultaneous 2D shape and topology inverse design with tuneable twig width (minimum thickness). Future improvements include a 3D filter generalization, an extension to probabilistic loads (varying in position, module and frequency) and further enrichment with embedded damage criteria (compliance element-wise penalization [22]).

Funding



This project has received funding from the European Union’s Horizon 2020 Marie Skłodowska-Curie Actions - Innovative European Training Networks under grant agreement No 956401, as well as from the Spanish Ministry of Science and Innovation and the State Research Agency (AEI) PID2021-126051OB-C43.

Conflict of interest

The authors declare that the research was conducted in the absence of any commercial or financial relationships that could be construed as a potential conflict of interest.

References

- [1] Erik Andreassen, Anders Clausen, Mattias Schevenels, Boyan S. Lazarov, and Ole Sigmund. Efficient topology optimization in matlab using 88 lines of code. *Structural and Multidisciplinary Optimization*, 43(1):1–16, November 2010.
- [2] Erik Andreassen, Boyan S. Lazarov, and Ole Sigmund. Design of manufacturable 3d extremal elastic microstructure. *Mechanics of Materials*, 69(1):1–10, February 2014.
- [3] Mauricio Arredondo-Soto, Enrique Cuan-Urquiza, and Alfonso Gómez-Espínosa. A review on tailoring stiffness in compliant systems, via removing material: Cellular materials and topology optimization. *Applied Sciences*, 11(8):3538, April 2021.
- [4] M.F Ashby. The properties of foams and lattices. *Philosophical Transactions of the Royal Society A: Mathematical, Physical and Engineering Sciences*, 364(1838):15–30, November 2005.
- [5] M. P. Bendsøe. Optimal shape design as a material distribution problem. *Structural Optimization*, 1(4):193–202, December 1989.
- [6] Martin Philip Bendsøe and Noboru Kikuchi. Generating optimal topologies in structural design using a homogenization method. *Computer Methods in Applied Mechanics and Engineering*, 71(2):197–224, November 1988.
- [7] M. P. Bendsøe and O. Sigmund. Material interpolation schemes in topology optimization. *Archive of Applied Mechanics (Ingenieur Archiv)*, 69(9–10):635–654, November 1999.
- [8] Blaise Bourdin. Filters in topology optimization. *International Journal for Numerical Methods in Engineering*, 50(9):2143–2158, February 2001.
- [9] Matteo Bruggi. On an alternative approach to stress constraints relaxation in topology optimization. *Structural and Multidisciplinary Optimization*, 36(2):125–141, January 2008.
- [10] Matteo Bruggi and Pierre Duysinx. Topology optimization for minimum weight with compliance and stress constraints. *Structural and Multidisciplinary Optimization*, 46(3):369–384, January 2012.
- [11] D.R. Carter and W.C. Hayes. Compact bone fatigue damage—i. residual strength and stiffness. *Journal of Biomechanics*, 10(5–6):325–337, January 1977.
- [12] D.R. Carter, W.C. Hayes, and D.J. Schurman. Fatigue life of compact bone—ii. effects of microstructure and density. *Journal of Biomechanics*, 9(4):211–218, January 1976.
- [13] Yonghua Chen, Jianan Lu, and Ying Wei. Topology optimization for manufacturability based on the visibility map. *Computer-Aided Design and Applications*, 13(1):86–94, August 2015.
- [14] Peter D. Dunning and H. Alicia Kim. Robust topology optimization: Minimization of expected and variance of compliance. *AIAA Journal*, 51(11):2656–2664, November 2013.

- [15] A. Díaz and O. Sigmund. Checkerboard patterns in layout optimization. *Structural Optimization*, 10(1):40–45, August 1995.
- [16] H. M. Frost. Bone “mass” and the “mechanostat”: A proposal. *The Anatomical Record*, 219(1):1–9, September 1987.
- [17] Erik Holmberg, Bo Torstenfelt, and Anders Klarbring. Stress constrained topology optimization. *Structural and Multidisciplinary Optimization*, 48(1):33–47, February 2013.
- [18] X. Huang, Z.H. Zuo, and Y.M. Xie. Evolutionary topological optimization of vibrating continuum structures for natural frequencies. *Computers and Structures*, 88(5–6):357–364, March 2010.
- [19] J. M. Hughes and M. A. Petit. Biological underpinnings of frost’s mechanostat thresholds: the important role of osteocytes. *Journal of Musculoskeletal and Neuronal Interactions (JMNI)*, 2(10):128–135, 2010.
- [20] R. Huiskes. If bone is the answer, then what is the question? *Journal of Anatomy*, 197(2):145–156, August 2000.
- [21] R. Huiskes, H. Weinans, H.J. Grootenhuis, M. Dalstra, B. Fudala, and T.J. Slooff. Adaptive bone-remodeling theory applied to prosthetic-design analysis. *Journal of Biomechanics*, 20(11–12):1135–1150, January 1987.
- [22] Luis Irastorza-Valera and Luis Saucedo-Mora. Probabilistic combination of loads in topology optimization designs via cumulative damage criteria, 2025.
- [23] Zhan Kang and Yiqiang Wang. Structural topology optimization based on non-local shepard interpolation of density field. *Computer Methods in Applied Mechanics and Engineering*, 200(49–52):3515–3525, December 2011.
- [24] Sun-Yong Kim. Constrained sensitivity filtering technique for topology optimization with lower computational expense. *International Journal for Numerical Methods in Engineering*, 124(18):4075–4096, June 2023.
- [25] S. Koppen. *Topology optimization of compliant mechanisms with multiple degrees of freedom*. PhD thesis, 2022.
- [26] Matthijs Langelaar. An additive manufacturing filter for topology optimization of print-ready designs. *Structural and Multidisciplinary Optimization*, 55(3):871–883, July 2016.
- [27] Matthijs Langelaar. Topology optimization of 3d self-supporting structures for additive manufacturing. *Additive Manufacturing*, 12:60–70, October 2016.
- [28] B. S. Lazarov and O. Sigmund. Filters in topology optimization based on helmholtz-type differential equations. *International Journal for Numerical Methods in Engineering*, 86(6):765–781, December 2010.
- [29] Boyan S. Lazarov, Fengwen Wang, and Ole Sigmund. Length scale and manufacturability in density-based topology optimization. *Archive of Applied Mechanics*, 86(1–2):189–218, January 2016.

- [30] Chau Le, Julian Norato, Tyler Bruns, Christopher Ha, and Daniel Tortorelli. Stress-based topology optimization for continua. *Structural and Multidisciplinary Optimization*, 41(4):605–620, October 2009.
- [31] Mark K. Leader, Ting Wei Chin, and Graeme J. Kennedy. High-resolution topology optimization with stress and natural frequency constraints. *AIAA Journal*, 57(8):3562–3578, August 2019.
- [32] Jikai Liu and Yongsheng Ma. A survey of manufacturing oriented topology optimization methods. *Advances in Engineering Software*, 100:161–175, October 2016.
- [33] A.G.M. Michell. The limits of economy of materials in frame-structures. *Phil Mag*, 8:589–597, 1904.
- [34] Igor Ostanin, Alexander Safonov, and Ivan Oseledets. Natural erosion of sandstone as shape optimisation. *Scientific Reports*, 7(1), December 2017.
- [35] Joakim Petersson and Ole Sigmund. Slope constrained topology optimization. *International Journal for Numerical Methods in Engineering*, 41(8):1417–1434, April 1998.
- [36] R. Picelli, W.M. Vicente, R. Pavanello, and Y.M. Xie. Evolutionary topology optimization for natural frequency maximization problems considering acoustic–structure interaction. *Finite Elements in Analysis and Design*, 106:56–64, November 2015.
- [37] Xiaoping Qian. Topology optimization in b-spline space. *Computer Methods in Applied Mechanics and Engineering*, 265:15–35, October 2013.
- [38] G. I. N. Rozvany. A critical review of established methods of structural topology optimization. *Structural and Multidisciplinary Optimization*, 37(3):217–237, February 2008.
- [39] G.I.N. Rozvany. Grillages of maximum strength and maximum stiffness. *International Journal of Mechanical Sciences*, 14(10):651–666, October 1972.
- [40] Luis Saucedo-Mora, Ismael Ben-Yelun, Hugo García-Modet, Miguel Ángel Sanz-Gómez, and Francisco Javier Montáns. The updated properties model (upm): A topology optimization algorithm for the creation of macro–micro optimized structures with variable stiffness. *Finite Elements in Analysis and Design*, 223:103970, October 2023.
- [41] M.B. Schaffler, E.L. Radin, and D.B. Burr. Long-term fatigue behavior of compact bone at low strain magnitude and rate. *Bone*, 11(5):321–326, January 1990.
- [42] Yu-Deok Seo, Hyun-Jung Kim, and Sung-Kie Youn. Isogeometric topology optimization using trimmed spline surfaces. *Computer Methods in Applied Mechanics and Engineering*, 199(49–52):3270–3296, December 2010.
- [43] Ole Sigmund. Morphology-based black and white filters for topology optimization. *Structural and Multidisciplinary Optimization*, 33(4–5):401–424, January 2007.
- [44] Ole Sigmund. Morphology-based black and white filters for topology optimization. *Structural and Multidisciplinary Optimization*, 33(4–5):401–424, January 2007.

- [45] M. Stolpe and K. Svanberg. An alternative interpolation scheme for minimum compliance topology optimization. *Structural and Multidisciplinary Optimization*, 22(2):116–124, September 2001.
- [46] Subodh C. Subedi, Chaman Singh Verma, and Krishnan Suresh. A review of methods for the geometric post-processing of topology optimized models. *Journal of Computing and Information Science in Engineering*, 20(6), June 2020.
- [47] S. Triambak, D.P. Mahapatra, N. Mallick, and R. Sahoo. A new logistic growth model applied to covid-19 fatality data. *Epidemics*, 37:100515, December 2021.
- [48] N. P. van Dijk, K. Maute, M. Langelaar, and F. van Keulen. Level-set methods for structural topology optimization: a review. *Structural and Multidisciplinary Optimization*, 48(3):437–472, March 2013.
- [49] Bin Wang and Denis Duhamel. On the design and optimization of acoustic network resonators for tire/road noise reduction. *Applied Acoustics*, 120:75–84, May 2017.
- [50] Michael Yu Wang, Xiaoming Wang, and Dongming Guo. A level set method for structural topology optimization. *Computer Methods in Applied Mechanics and Engineering*, 192(1–2):227–246, January 2003.
- [51] H. Weinans, R. Huiskes, and H.J. Grootenboer. The behavior of adaptive bone-remodeling simulation models. *Journal of Biomechanics*, 25(12):1425–1441, December 1992.
- [52] Julius Wolff. *Das Gesetz der Transformation der Knochen (The Law of Bone Remodelling)*. Springer Berlin Heidelberg, 1892.
- [53] R. J. Yang and C. J. Chen. Stress-based topology optimization. *Structural Optimization*, 12(2–3):98–105, October 1996.
- [54] Bing Yi, Gil Ho Yoon, Ran Zheng, Long Liu, Daping Li, and Xiang Peng. A unified material interpolation for topology optimization of multi-materials. *Computers and Structures*, 282:107041, July 2023.
- [55] Benliang Zhu, Xianmin Zhang, Hongchuan Zhang, Junwen Liang, Haoyan Zang, Hai Li, and Rixin Wang. Design of compliant mechanisms using continuum topology optimization: A review. *Mechanism and Machine Theory*, 143:103622, January 2020.
- [56] Jihong Zhu, Han Zhou, Chuang Wang, Lu Zhou, Shangqin Yuan, and Weihong Zhang. A review of topology optimization for additive manufacturing: Status and challenges. *Chinese Journal of Aeronautics*, 34(1):91–110, January 2021.
- [57] Wenjie Zuo and Kazuhiro Saitou. Multi-material topology optimization using ordered simp interpolation. *Structural and Multidisciplinary Optimization*, 55(2):477–491, June 2016.